Journal of Materials Chemistry C

PAPER

View Article Online
View Journal | View Issue

Cite this: J. Mater. Chem. C, 2015, 3, 11635

A charge neutral iron(II) complex with an above room temperature spin crossover (SCO) and hysteresis loop†

Kuppusamy Senthil Kumar,[a] Ivan Šalitroš,[b] Benoît Heinrich,[a] Olaf Fuhr[c] and Mario Ruben*[ac]

We report on the unusually abrupt spin crossover (SCO) behaviour of a tridentate-nitrogen pyrazole–pyridine–tetrazole ($\mathbf{L^1H}$) based charge-neutral [$\mathbf{Fe(L^1)_2}$] complex. Different reaction conditions were utilized to prepare the complex in crystalline and powder forms. X-ray crystallographic analysis of the complex at 180 K revealed distorted tetragonal bipyramidal geometry around the Fe(II) coordination center with Fe–N bond lengths and angles indicative of the low spin state of the complex. Investigation of the magnetic behaviour of the powder and crystalline forms of the complex yielded an abrupt and above room temperature first order SCO ($T_{1/2\downarrow}$ = 346.3 K and $T_{1/2\uparrow}$ = 349 K) with an ~2.6 K hysteresis loop for the powder sample, whereas the crystalline form remained in the low spin state throughout the measurement temperature range. Upon irradiation with red or green light (λ = 637 nm or 532 nm, 10 mW cm^{-2}) the powder form of the complex showed a light-induced excited spin state trapping (LIESST) effect with a $T_{(LIESST)}$ value of 63 K, and no LIESST effect was observed for the crystalline complex. Reversible phase transition and large enthalpy (ΔH) and entropy (ΔS) changes associated with SCO of [$\mathbf{Fe(L^1)_2}$] were inferred from differential scanning calorimetry (DSC) experiments. This was corroborated by variable temperature small angle X-ray scattering (SAXS) measurements wherein different crystalline phases associated with LS and HS [$\mathbf{Fe(L^1)_2}$] complexes and their reversible inter-conversion upon SCO were unambiguously observed.

Received 9th July 2015,
Accepted 18th September 2015

DOI: 10.1039/c5tc02079d

www.rsc.org/MaterialsC

Introduction

A reversible change in the spin state of a coordination complex from low spin (LS) to high spin (HS) affected by the application of external stimuli such as temperature, pressure, light, and magnetic and electric fields is defined as the spin crossover (SCO).[1] The occurrence of the hysteresis loop[2] and the change in physical properties such as colour[3] and electrical conductivity[4] upon SCO render the SCO active complexes suitable for switching and memory applications.[5] Ever since the first observation of the SCO phenomenon in a molecular Fe(III) complex,[6] a large number of SCO active complexes were reported with majority of them falling under the category of metal ions having 3d^4–3d^7 electronic configuration.[7] Among them, the 3d^6 Fe(II) ion coordinated with all nitrogen or mixed nitrogen–oxygen donor ligand systems of moderate field strength gained a lot of attention due to their facile inter-conversion from the diamagnetic (S = 0) low spin (LS) state to the paramagnetic (S = 2) high spin (HS) state upon application of external stimuli.[8] Research towards synthesis of Fe(II) based counter-anion free charge neutral complexes is gaining increasing attention due to their attractive magnetic properties coupled with propensity to sublime to form thin 2D film essential for device fabrication.[9] A range of SCO active charge neutral complexes were reported and their magnetic properties in bulk and thin films were investigated.[10] To further build on in this direction, we designed a 2-(1*H*-pyrazol-1-yl)-6-(1*H*-tetrazol-5-yl)pyridine (**LH**) ligand (*cf.* Scheme 1) and reported room temperature SCO behaviour of the corresponding charge neutral Fe(II) complex [$\mathbf{Fe(L)_2}$] in bulk and 2D film[11] and its capability to sense ethanol and methanol solvents based on its solvatochromic spin state switching.[12] Also, Pati and co-workers recently predicted large magnetoresistance,

[a] Institut de Physique et Chimie des Matériaux de Strasbourg (IPCMS), CNRS-Université de Strasbourg, 23, rue du Loess, BP 43, 67034 Strasbourg cedex 2, France. E-mail: mario.ruben@kit.edu
[b] Institute of Inorganic Chemistry, Technology and Materials, Faculty of Chemical and Food Technology, Slovak University of Technology, Bratislava, 81237, Slovak Republic
[c] Institute of Nanotechnology, Karlsruhe Institute of Technology (KIT), Hermann-von-Helmholtz-Platz 1, 76344, Eggenstein-Leopoldshafen, Germany

† Electronic supplementary information (ESI) available: UV-vis, photoluminescence and photoluminescence excitation spectra of ligands and complexes. CCDC 1063582. For ESI and crystallographic data in CIF or other electronic format see DOI: 10.1039/c5tc02079d

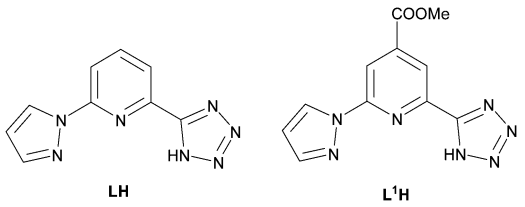

Scheme 1 Molecular structures of 2-pyrazol-1-yl-6-(1*H*-tetrazol-5-yl)-pyridine (**LH**) and 2-pyrazol-1-yl-6-(1*H*-tetrazol-5-yl)-isonicotinic acid methyl ester (**L^{1}H**) ligands.

efficient conductance-switching and spin-filter activity for [**Fe(L)$_2$**] embedded in a nano-junction.[13]

To further expand the scope of the aforementioned **LH** ligand system, a synthetic strategy was developed and a novel 2-pyrazol-1-yl-6-(1*H*-tetrazol-5-yl)-isonicotinic acid methyl ester (**L^{1}H**) ligand system (*cf.* Scheme 1) with a COOMe functional group at the 4 position of the pyridine ring amenable to further functionalization was synthesized. In this work we describe the SCO active nature of the Fe(II) complex [**Fe(L^1)$_2$**] based on the **L^{1}H** ligand and various factors governing its SCO behaviour.

Results

Synthesis

The synthesis of ligand **L^{1}H** was carried out starting from 2,6-dibromo-isonicotinic acid methyl ester as shown in Scheme 2. An improved synthetic pathway was developed to introduce the pyrazole group in a facile manner following a procedure reported by Zeng *et al.*[14] yielding the expected mono-substituted compound **2** in two hours (TLC control) from the dibromo compound **1** without affecting the COOMe functional group. The syntheses of compounds **3** and **L^{1}H** were performed based on a previously reported procedure. Wherein, lanthanide (Eu^{3+} and Tb^{3+}) luminescence sensitization efficiency of **L^{1}H** was detailed.[15] The charge-neutral [**Fe(L^1)$_2$**] complex was prepared from **L^{1}H** in crystalline and powder forms as depicted in Scheme 2 (conditions d and e).

The addition of an equimolar amount of Et_3N to a dilute solution of **L^{1}H** (0.9 mg ml^{-1}) in the DCM/MeOH solvent mixture (Scheme 2, condition d) resulted in the formation of anionic L^{1-}, further reaction of this species with the Fe(II) precursor resulted in a clear dark red solution. Slow evaporation of this solution over the period of 2–3 weeks under ambient conditions yielded dark red block single crystals of [**Fe(L^1)$_2$**] suitable for X-ray diffraction. When the coordination reaction was performed in a concentrated solution of **L^{1}H** (5.4 mg ml^{-1}) in the DCM/MeOH solvent mixture (Scheme 2, condition e), an immediate precipitation occurred, and the filtration of this precipitate followed by drying under vacuum yielded an analytically pure [**Fe(L^1)$_2$**] complex as a red powder. The powder and crystalline forms of the complex feature extremely low solubility in common organic solvents except dimethyl sulfoxide (DMSO) prohibiting meaningful solution phase nuclear magnetic resonance (NMR) studies. Nevertheless, solution phase NMR measurements performed in the 7 : 3 $CHCl_3/CH_3OH$ solvent mixture in which the complex is sparingly soluble revealed

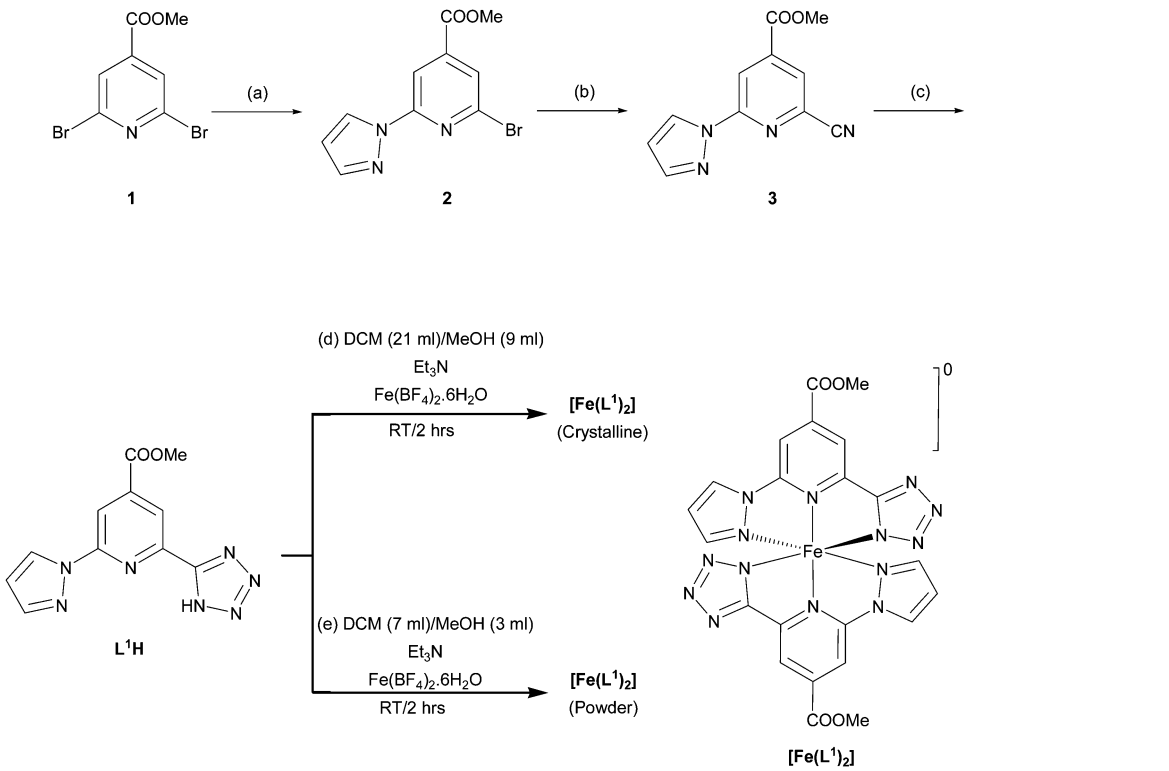

Scheme 2 Synthesis of ligand **L^{1}H** and the [**Fe(L^1)$_2$**] complex; reaction conditions: (a) 1,10-phenanthroline, CuI, pyrazole and K_2CO_3 in toluene, 120 °C, under Ar, 2 h; (b) CuCN in DMF, 150 °C, under Ar, 2 h; (c) NaN_3/NH_4Cl in DMF, 130 °C, 4 h (see also the Experimental section).

the low spin state of the complex as depicted in Fig. S1 (ESI†), wherein all the peaks corresponding to the complex moiety were observed below 12 ppm and no signals corresponding to the high spin complex were observed in the downfield region of the spectrum even after 2048 scans as previously reported for [**Fe(L)$_2$**].[11] The NMR spectrum recorded in DMSO is also indicative of the low spin state of the complex as depicted in Fig. S2 (ESI†).

Crystallographic analysis

The single crystal X-ray diffraction analysis has been performed on the crystalline form of the complex [**Fe(L^1)$_2$**]. This polymorph crystallized in a monoclinic crystal system with the *C*2/*c* space group (Table 1), and a coordination number of 6 was obtained with three nitrogen atoms from each ligand donating electron density to the Fe(II) ion in a distorted octahedral coordination geometry as shown in Fig. 1a.

The unit cell contains four [**Fe(L^1)$_2$**] complex units. The Fe1–N1(pyrazole), Fe1–N3(pyridine) and Fe1–N4(tetrazole) bond lengths (Fig. 1a) obtained at 180 K clearly indicate the LS state of the Fe(II) ion, and these values are similar to the bond lengths of the previously reported parent charge neutral complex.[11] The N1(pyrazole)–Fe1–N4(tetrazole) bond angle of 160.38(7)° also indicates the LS state (*ca.* 160° for LS and 145° for HS in analogous systems) of the central metal ion, interestingly the present system is slightly more symmetric in comparison with the parent complex [**Fe(L)$_2$**], wherein two different angles of 160.04(14)° and 159.83(14)° were observed for pyrazole–Fe–tetrazole bonds.[11] To gain an insight into the intermolecular interactions between the complex molecules, the unit cell packing pattern of the [**Fe(L^1)$_2$**] complex was analysed as depicted in Fig. 1b. Two different intermolecular interactions between the complex skeletons were observed, namely, (i) interaction between pyridine hydrogen and tetrazole nitrogen with a distance of 2.46(3) Å (red) and (ii) interactions between tetrazole nitrogen and hydrogen atoms of the pyrazole ring with a distance of 2.27(1) Å (purple).

Table 1 Crystallographic data of [**Fe(L^1)$_2$**][a]

Formula	$C_{22}H_{16}FeN_{14}O_4$	V/Å^3	2457.1(2)
FW/g mol^{-1}	596.34	Z	4
T/K	180.15	ρ/g cm^{-3}	1.612
Crystal system	Monoclinic	μ/mm^{-1}	0.677
Space group	*C*2/*c*	θ min-max/°	2.31–25.582
a/Å	16.2431(8)	Reflns collected	2306
b/Å	10.5762(3)	Indep reflns	2298
c/Å	14.6113(8)	Parameters	188
α/°	90	GOF on F^2	1.044
β/°	101.796(4)	R_1	0.0305
γ/°	90	wR_2	0.0709

[a] CCDC 1063582.

As discussed in the Introduction section, these intermolecular interactions may play an important role in determining the magnetic properties of the [**Fe(L^1)$_2$**] complex, *vide infra*.

Photophysical properties of L^{1}H and [Fe(L^1)$_2$]

Electronic absorption and photoluminescence (PL) characteristics

UV-vis absorption spectra of the **L^{1}H** ligand and the [**Fe(L^1)$_2$**] complex were recorded in the 7 : 3 DCM/MeOH solvent mixture as depicted in Fig. 2a. Both the ligand and the complex showed strong $^1(\pi \rightarrow \pi)$ absorption bands at around 235, 263 and 326 nm (Fig. 2a). The absorption maxima of the complex are slightly bathochromically shifted (~3–4 nm) in comparison to the ligand.

Apart from the intense transitions in the UV region due to the ligand, the complex also showed a parity and spin allowed metal to ligand charge transfer transition ^{1}(MLCT) band at

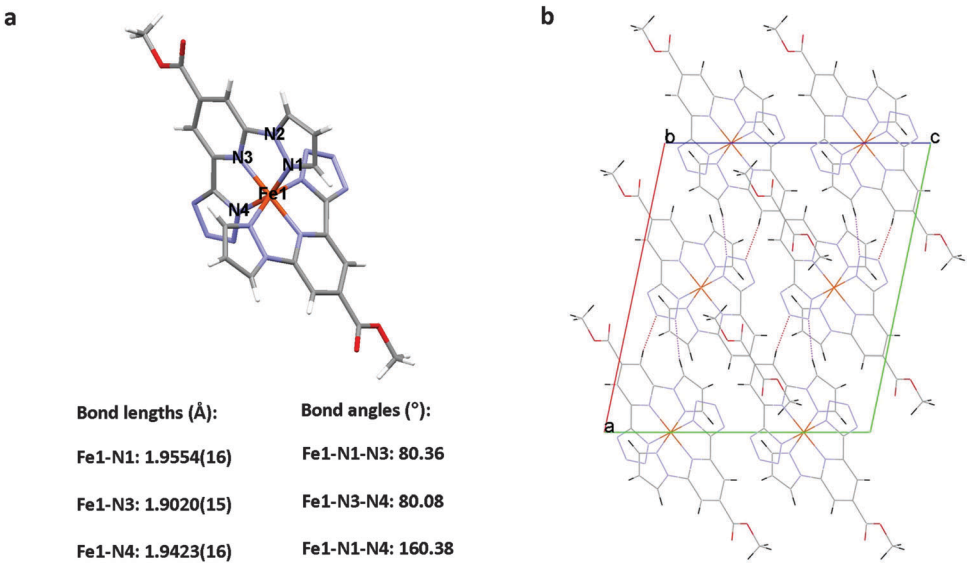

Fig. 1 (a) Stick diagram of the [**Fe(L^1)$_2$**] complex viewed down the crystallographic *b* axis and (b) unit cell packing pattern viewed down the crystallographic *b* axis; intermolecular interactions are represented with dotted lines of different colours.

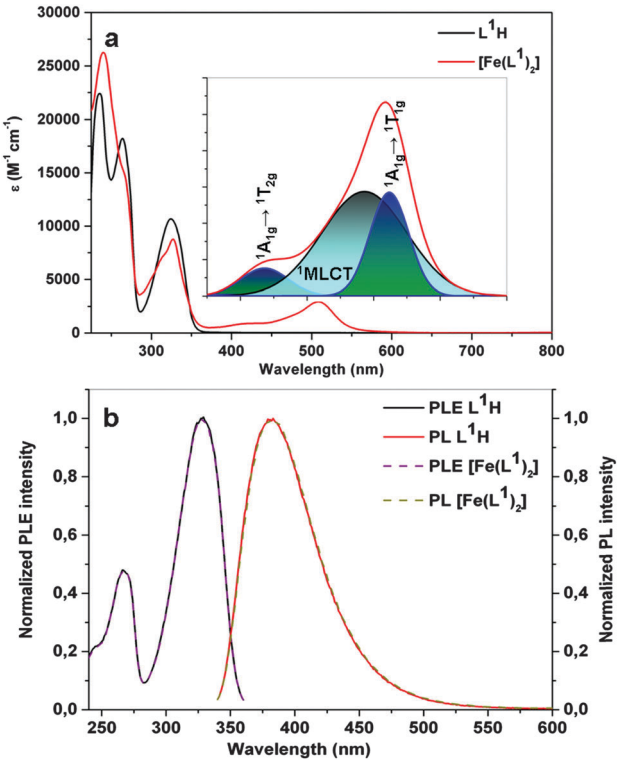

Fig. 2 (a) UV-vis absorption spectra and (b) PLE and PL spectra of $\mathbf{L^1H}$ and $\mathbf{[Fe(L^1)_2]}$ in the DCM/MeOH solvent mixture; the PL and photoluminescence excitation (PLE) spectra were excited and recorded at 326 and 383 nm. The inset of (a) shows the Gaussian deconvoluted spectrum of d–d and the MLCT region of $\mathbf{[Fe(L^1)_2]}$.

493 nm as inferred from the Gaussian deconvolution of the 390–600 nm spectral region (Fig. 2a, inset). This indicates the energetically more stabilized nature of the ligand centered π* orbital in $\mathbf{[Fe(L^1)_2]}$ compared to the parent **LH** ligand based complex (^{1}MLCT at 450 nm, *cf.* Fig. S3, ESI†) attributed to the mesomeric effect of the COOMe substituent. Upon deconvolution, parity forbidden d–d transitions centred at 512 nm ($^1A_{1g} \rightarrow {}^1T_{1g}$) and 416 nm ($^1A_{1g} \rightarrow {}^1T_{2g}$) corresponding to the Fe(II) ion in a distorted octahedral ligand field can be clearly visualized as depicted in the inset of Fig. 2a.

Upon excitation of the $^1(\pi \rightarrow \pi)$ band located at 327 nm, the ligand showed bright fluorescence with the maximum located at 383 nm. A quantum yield of 61% and a Stokes shift of 56 nm were estimated. The PL and photoluminescence excitation (PLE) profiles of the $\mathbf{[Fe(L^1)_2]}$ complex remained identical to those of the ligand compound (Fig. 2b and Fig. S4, ESI†) with a slightly reduced PL quantum yield (*cf.* Table 2) elucidating negligible coupling between the spin state and luminescence in solution. Also, the similar nature of absorption and PLE spectra observed for both the ligand and the complex (Fig. S5a and b, ESI†) clearly indicate the absence of excited state phenomena such as excimer and exciplex formation. For the occurrence of coupling between the spin state and luminescence in solution with the complex in the low spin state, energy transfer (antenna effect) from the ligand centred $^1(\pi \rightarrow \pi)$ state to ^{1}(MLCT) and its subsequent intersystem crossing to the

Table 2 Absorption maxima (λ_{max}), molar absorptivity coefficients (ε) and photoluminescence (PL) quantum yields of the ligand and the complex measured in the 7 : 3 DCM/MeOH solvent mixture under ambient conditions

Molecule	λ_{max} nm^{-1} ($\varepsilon/10^{-4}$ cm^{-1} M^{-1})	Q_F[a]
$\mathbf{L^1H}$	235 (2.2), 263 (1.8), 324 (1.1)	0.61
$\mathbf{[Fe(L^1)_2]}$	239 (2.6), 266 (1.5), 327 (0.88), 417 (0.098), 507 (0.29)	0.54

[a] Pyrene as standard and average of three independent measurements.

^{3}(MLCT) state are prerequisites which in turn will quench the ligand centred fluorescence analogues to the mechanism extensively reported for Ru(II) complexes.[16] This mechanistic pathway is feasible in Ru(II) complexes because the "heavy" Ru(II) facilitates intersystem crossing (ISC) from ^{1}(MLCT) to ^{3}(MLCT) *via* spin–orbit coupling[17] as against "light" Fe(II) in which such an effect is not strong enough to facilitate ISC; this may have affected the similar photophysical properties observed for $\mathbf{L^1H}$ and $\mathbf{[Fe(L^1)_2]}$ systems. To prove this facet, the corresponding Ru complex, $\mathbf{[Ru(L^1)_2]}$, was synthesized (see ESI† for details) and its photophysical properties were investigated as depicted in Fig. S6a and b (ESI†). As expected, the ligand centred fluorescence in $\mathbf{[Ru(L^1)_2]}$ is clearly quenched in comparison to $\mathbf{[Fe(L^1)_2]}$ indicating intersystem crossing in $\mathbf{[Ru(L^1)_2]}$ but with no apparent phosphorescence from ^{3}(MLCT) for reasons extensively discussed in the literature.[18] Also, we have recently reported lanthanide (Eu^{3+} and Tb^{3+}) luminescence sensitization efficiency of $\mathbf{L^1H}$ which in part is facilitated by "heavy" lanthanide ions clearly confirming the important role of the heavy atom effect in modulating energy transfer dynamics in metal complexes.[15] Based on the above facets, the similar photophysical properties observed for the ligand and the complex in solution could be tentatively attributed to the lack of spin–orbit coupling in the $\mathbf{[Fe(L^1)_2]}$ complex which in turn did not facilitate energy transfer leading to quenching/modulation of luminescence. A careful look at the literature confirms the afore-reached conclusion; for example, Halcrow and co-workers reported Fe(II) SCO complexes based on tridentate indazolylpyridine ligands and showed that the ligand centered PL is retained in complexes which clearly indicates the absence of coupling between the spin state and luminescence in solution as observed in this work,[19] see also a report by Zigler *et al.* detailing "electronic uncoupling" between the Fe(II) metal centre and the anthracene modified bipyridine ligand for similar behaviour discussed above.[20] In retrospect, there are reports detailing coupling between the spin state and luminescence in the solid state,[21] except in very few cases where the mechanistic aspects were not clearly established. Thus to realize complexes featuring coupling between the spin state and luminescence in solution, the problem has to be approached from a different conceptual viewpoint as detailed in a recent study reported by Weber and co-workers, wherein a Ni^{2+} complex capable of undergoing change in geometry upon addition of the pyridine ligand led to the realization of synergy between the spin state and luminescence in solution.[22] It is also remarkable that, upon moving from the solution to solid state

the situation may be drastically different especially in the case of SCO systems grafted with polycyclic aromatic fluorophores such as pyrene whose PL can be tuned with respect to the spin state due to varying intermolecular interactions upon switching as reported by Bousseksou and co-workers[23] and Tao and co-workers.[24] This facet is still needed to be substantiated for molecular SCO complexes as reported by Garcia *et al.*,[21a] hence it is worthwhile to study the photophysical properties of the $[\mathbf{Fe(L^1)_2}]$ complex in the solid state.

To gain a preliminary insight into the PL of powder $[\mathbf{Fe(L^1)_2}]$ in the solid state at room temperature where the complex is in the LS state, the ligand centred $^1(\pi \rightarrow \pi)$ band of the complex located at 334 nm (Fig. S7a, ESI†) was excited; remarkably, the $[\mathbf{Fe(L^1)_2}]$ complex showed very weak PL in comparison to $\mathbf{L^1H}$ as depicted in Fig. S7b (ESI†). Further investigations are on to understand this behaviour and the details will be reported elsewhere.

Magnetic properties of $[\mathbf{Fe(L^1)_2}]$

Magnetic measurements of the crystalline form of $[\mathbf{Fe(L^1)_2}]$ revealed LS state diamagnetic behaviour up to 400 K temperature as depicted in Fig. S8 (ESI†). Interestingly, the powder sample exhibited abrupt first order SCO with 3.3 K and 2.7 K hysteresis loops for first ($T_{1/2\downarrow}$ = 345.5 K and $T_{1/2\uparrow}$ = 348.8 K) and second scans ($T_{1/2\downarrow}$ = 346.3 K and $T_{1/2\uparrow}$ = 349 K; Fig. 3a). Further scanning resulted in stabilized SCO behavior similar to the second scan (data not shown). The presence of the lattice water molecule and its subsequent removal upon first heating could explain the shifted first scan behaviour. The obtained values of the χT product of 3.55 cm^3 K mol^{-1} and 0.16 cm^3 K mol^{-1} at 365 K and 336 K indicate the presence of pure high and low spin species at those temperatures and genuine temperature-induced SCO behaviour. More than 90% of iron(II) central atoms undergo SCO within the 3.3 K interval in heating and within the 4 K interval in cooling mode, which proves unusually sharp SCO of the powder sample of $[\mathbf{Fe(L^1)_2}]$. The abruptness associated with the SCO of $[\mathbf{Fe(L^1)_2}]$ could be attributed to the strong cooperative intermolecular interactions present between the complex molecules in the lattice as in the case of $[\mathbf{Fe(L)_2}]$.

For photomagnetic experiments, both crystalline and powder samples of $[\mathbf{Fe(L^1)_2}]$ were prepared as thin layers to ensure sample saturation upon irradiation. Samples were slowly cooled down to 10 K which results in switching of the sample into the LS state and an external magnetic field of 0.1 T was applied. In the case of the powder sample of $[\mathbf{Fe(L^1)_2}]$, red or green light irradiation (λ = 637 nm or 532 nm, 10 mW cm^{-2}) caused an increase of the magnetic moment and when the saturation point has been reached, the light was switched off. Red laser light was more efficient in the photoexcitation to the high spin state and after about 120 minutes of irradiation magnetic moment reached saturation. The photoexcitation of the sample caused an increase of the χT product up to 2.3 cm^3 K mol^{-1}, which corresponds to 64% of iron(II) central atoms of the HS state (Fig. 3b, blue triangles). The increase of temperature above 55 K results in a decreasing χT product which finally undergoes a complete thermal relaxation to the LS ground spin state (Fig. 3b, green squares). The T (LIESST)

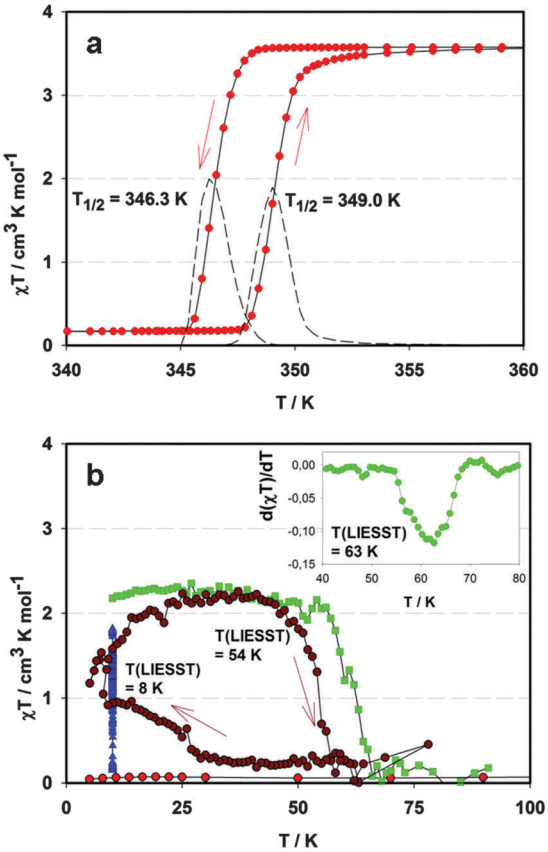

Fig. 3 Magnetic properties of the powder form of $[\mathbf{Fe(L^1)_2}]$: (a) Standard measurements in the dark: red circles – χT *vs.* T curve in the dark; dashed line – d(χT)/dT *vs.* T curve; (b) photomagnetic properties: red circles – measurement in the dark recorded before light irradiation; blue triangles light irradiation (λ = 637 nm, 10 mW cm^{-2}) at 10 K; green squares – data recorded in the warming mode and in the dark after irradiation (LIESST curve); brown circles – data recorded in the warming and in the cooling mode under permanent light irradiation (LITH curve), inset: d(χT)/dT *vs.* T dependence calculated from the LIESST curve.

value, calculated from the minimum in the $\partial(\chi T)/\partial T$ *vs.* T curve, was determined to be 63 K. In order to learn more about the photo-induced bistability of the HS $[\mathbf{Fe(L^1)_2}]$, the light-induced thermal hysteresis (LITH)[25] behavior of the complex was investigated (Fig. 3b, brown circles). In LITH experiments, the sample was irradiated at 10 K until saturation of the magnetic signal was reached, then the temperature was slowly elevated up to 90 K under permanent irradiation and consequently cooled down back to 10 K. According to the calculated x_{HS} fraction, 50% of photo-excited HS molecules exist at 54 K in the heating and at 8 K in the cooling mode. Thus, the experiment reveals at around 10 K the width of light-induced thermal hysteresis proving that the photo-trapped HS phase displays a considerable degree of cooperativity. In the case of the crystalline form of $[\mathbf{Fe(L^1)_2}]$, no photo-magnetic response at both wavelengths was observed.

Analysis of the SCO phenomenon of powder $[\mathbf{Fe(L^1)_2}]$

To investigate the interesting magnetic behavior observed for the powder sample, differential scanning calorimetry (DSC) and

small angle X-ray scattering (SAXS) studies were carried out as detailed below.

DSC analysis

DSC measurements were performed to shed light on the phase, enthalpy (ΔH) and entropy (ΔS) changes associated with the SCO event. A C_p *vs.* T plot of the powder sample showed two maxima (T_1^{up} = 378.5 K and T_2^{up} = 383 K) in the heating (endothermic) mode and one maximum (T_1^{down} = 351.5 K) in the cooling mode (exothermic) in the first cycle as depicted in Fig. 4a.

In the second cycle, a single maximum was resulted in both heating and cooling modes as shown in Fig. 4b, importantly, the endothermic (T_1^{up} = 347.1 K) and exothermic (T_1^{down} = 344.4 K) peak maxima were shifted to lower temperatures in comparison to the first cycle with a pronounced temperature shift observed for the endothermic process. Subsequent scanning resulted in stable thermal behavior analogous to the magnetic behavior discussed in the previous section. The presence of two endothermic peaks in the first scan could be attributed to the release of the lattice water molecule and the phase change associated with the complex upon SCO; this was corroborated by the absence of the second peak at the second cycle and 1.3 water molecules observed in elemental analysis of the powder [**Fe(L^1)$_2$**] complex (*vide infra*). The close correlation between magnetic measurements and DSC analysis, especially the similar hysteresis values obtained from both measurements (Table 3), clearly indicates an occurrence of reversible phase transition in the [**Fe(L)$_2$**] complex upon conversion from LS to HS and *vice versa*.

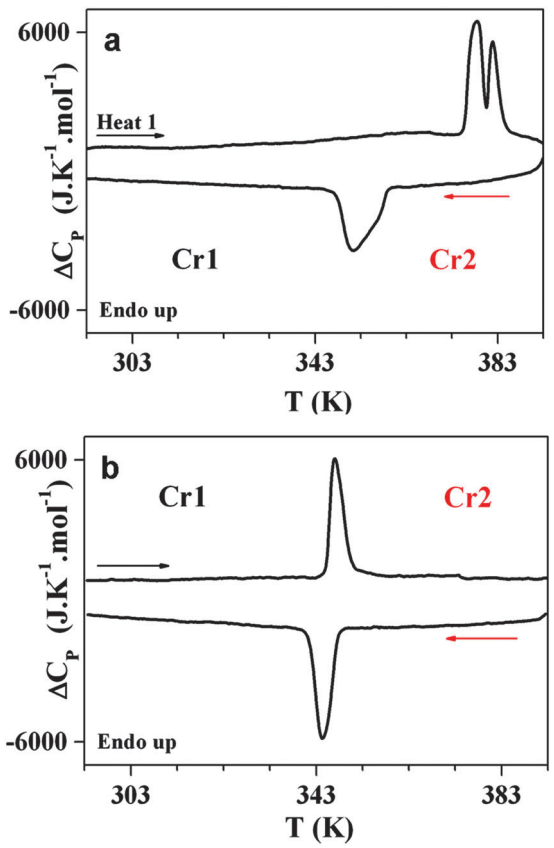

Fig. 4 Heat capacity *vs.* T plot for the powder form of the [**Fe(L^1)$_2$**] complex at (a) first and (b) second scans.

Table 3 Thermodynamic parameters associated with the SCO of the [**Fe(L^1)$_2$**] complex

Parameter[a]	SQUID	DSC
T_1^{up} (K)	348.9	347.1
T_1^{down} (K)	346.3	344.4
ΔT (K)	2.6	2.7
ΔH^{up} (kJ mol^{-1})		19.3
ΔH^{down} (kJ mol^{-1})		20.3
ΔS^{up} (J K^{-1} mol^{-1})		55.5
ΔS^{down} (J K^{-1} mol^{-1})		58.9

[a] From the second cycle.

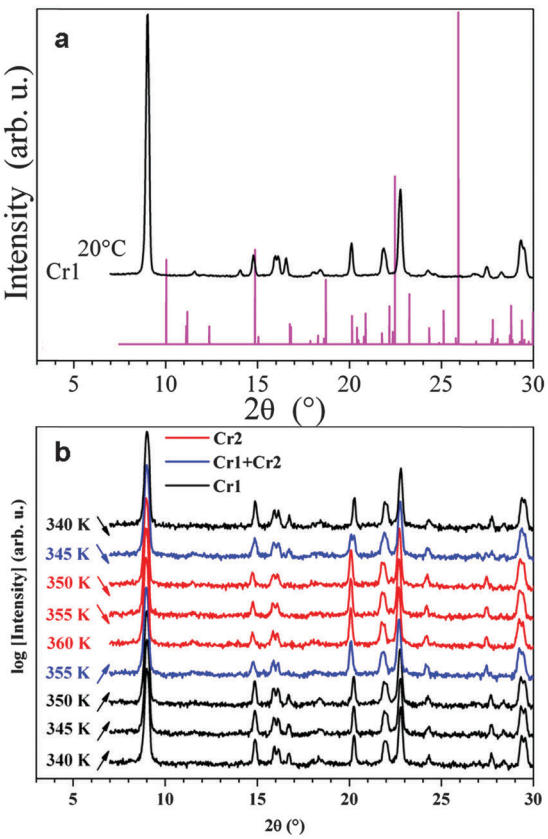

Fig. 5 (a) Comparison between SAXS and simulated X-ray diffraction patterns of the [**Fe(L^1)$_2$**] complex in powder and crystalline forms and (b) Variable temperature SAXS patterns of the [**Fe(L^1)$_2$**] complex in powder form. The notations Cr1 and Cr2 represent crystalline phases associated with LS and HS states.

The estimated enthalpy (ΔH) and entropy (ΔS) values of 20 kJ mol^{-1} and 55 J K^{-1} mol^{-1} for the powder sample fall in the range of typical values observed for iron(II) SCO complexes (ΔH = 3–27 kJ mol^{-1} and ΔS = 22–94 J K^{-1} mol^{-1}). Furthermore, the ΔS values of 55.5 and 58.9 J K^{-1} mol^{-1} obtained for the SCO event in heating and cooling mode clearly indicate a significant

contribution from the vibrational entropy along with the entropy gain arising from the changes in the electronic structure (ΔS_{el} = 13 J K^{-1} mol^{-1}).

SAXS studies

To further investigate the phase transition associated with SCO, SAXS studies were carried out around the SCO region inferred from magnetic measurements. A comparison between the powder SAXS pattern obtained at 293.15 K and the simulated pattern obtained from the single crystal X-ray diffraction study at 180 K clearly indicates completely different structures present in powder and crystalline samples of the $[\mathbf{Fe(L)_2}]$ complex as depicted in Fig. 5a.

From the data depicted in Fig. 5b a clear phase transition occurring between 340.15 K and 350.15 K could be inferred along with 10 K hysteresis between both crystal phases.

Discussion

The temperature-dependent investigation of the magnetic properties of the parent crystalline $[\mathbf{Fe(L)_2}]$ complex revealed an abrupt room temperature SCO with a stable thermal hysteresis loop of 5 K width ($T_{1/2\downarrow}$ = 292 K, $T_{1/2\uparrow}$ = 297 K), in the presence of hydrogen bonded methanol molecules in the crystal lattice and associated weakening of the ligand field is a factor leading to the room temperature SCO in the case of $[\mathbf{Fe(L)_2}]$.[11] Upon modification of the parent skeleton with the COOMe group, remarkable changes in the SCO behavior was observed. Unlike $[\mathbf{Fe(L)_2}]$, the crystalline form of $[\mathbf{Fe(L^1)_2}]$ was trapped in the low spin state and failed to show SCO both under thermal and light irradiation conditions. Remarkably, the powder form of $[\mathbf{Fe(L^1)_2}]$ showed an abrupt and above RT SCO with a slightly lower 2.6 K hysteresis loop in comparison with $[\mathbf{Fe(L)_2}]$. Strong intermolecular interactions present in crystalline $[\mathbf{Fe(L^1)_2}]$ could be a reason behind locking the complex in the low spin state, whereas, reduced intermolecular interactions in the powder form of $[\mathbf{Fe(L^1)_2}]$ may have facilitated the temperature and light induced SCO. A recent report by Naggert *et al.*[26] clearly elucidated the role of intermolecular interactions in modulating the SCO of charge neutral Fe(II) complexes based on substituted penanthroline and dihydrobis(pyrazolyl)borate ligands, wherein, the formation of dimers through intermolecular π–π interactions trapped the crystalline complex in the high spin state, conversely, the powder form showed an incomplete SCO due to reduced intermolecular interactions. From the above experimental observations, it can be clearly interpreted that too strong intermolecular interactions between the complex entities may obstruct the occurrence of SCO and hence judicious interaction strength has to be maintained in order to allow SCO to occur through volume expansion of the complex upon switching from the LS to HS state.

The powder form of $[\mathbf{Fe(L^1)_2}]$ also showed the LIESST effect which is more pronounced upon irradiation with the red laser (λ = 637 nm) than green laser (λ = 532 nm). Direct population of the $^3T_2$ level from the $^1A_1$ level could be tentatively attributed to the efficient LIESST effect observed for lower wavelength (637 nm) excitation in analogy with the reported mechanism for tetrazole based systems.[27]

Another remarkable feature associated with the SCO of $[\mathbf{Fe(L^1)_2}]$ is the reversible phase change upon transition from LS to HS and *vice versa* leading to hysteretic SCO behaviour, an important property needed to be tamed to realize molecular memory devices based on SCO complexes. The present $\mathbf{L^1H}$ system with potential for further functionalization is handy towards building of functional charge neutral SCO complexes; efforts are in progress in this direction.

Conclusions

Extending on our previous report detailing a charge neutral Fe(II) SCO complex, we developed a facile synthetic pathway leading to the $\mathbf{L^1H}$ ligand system with an added COOMe functional group. The powder form of the $[\mathbf{Fe(L^1)_2}]$ complex showed first order abrupt SCO behavior well above room temperature with a 2.6 K hysteresis loop. Photo-switching of the spin state at 10 K was also observed for the powder form of the $[\mathbf{Fe(L^1)_2}]$ complex with a $T_{(LIESST)}$ value of 63 K. Conversely, the crystalline form of the $[\mathbf{Fe(L^1)_2}]$ complex failed to show both thermal and light induced SCO attributed to the strong intermolecular interactions which froze the complex in the LS state. The large enthalpy and entropy changes associated with the SCO of the powder form of the $[\mathbf{Fe(L^1)_2}]$ complex clearly indicate a phase change mediated hysteretic SCO. The reversible nature of the phase change associated with the SCO event is unambiguously supported by SAXS investigations, wherein two different structures of the $[\mathbf{Fe(L^1)_2}]$ complex in its low and high spin states were clearly observed. The uncharged molecular character of the $[\mathbf{Fe(L^1)_2}]$ complex and its excellent photo-physical properties, especially PL quantum efficiency in the range of 60%, make it a suitable candidate for studying possible phase change mediated synergetic coupling between the spin state and PL in the solid state: efforts are on in this direction.[28,29]

Experimental section

Materials and methods

Anhydrous solvents, 1,10-phenanthroline monohydrate, CuI, Et_3N, K_2CO_3, $Fe(BF_4)_2{\cdot}6H_2O$ and $Ru(DMSO)_4Cl_2$ were purchased from commercial sources and used as received. Glassware is dried in a vacuum oven at 150 °C prior to the experiments. All the complexation reactions were performed under an argon (Ar) atmosphere.

Synthesis

Synthesis of 2-bromo-6-pyrazol-1-yl-isonicotinic acid methyl ester (2). To 50 ml of dry and Ar bubbled toluene in a dry 250 ml two-neck flask, methyl-2,6-dibromoisonicotinate **1** (2.65 g, 9 mmol), pyrazole (1.23 g, 18 mmol), 1,10-phenanthroline monohydrate (0.177 g, 0.9 mmol, 10 mol%), CuI (0.171 g, 0.9 mmol, 10 mol%) and K_2CO_3 (2.74 g, 18 mmol) were added

and stirred at 120 °C for 2 h. After cooling to room temperature, the mixture was filtered through celite, and the solvent was removed under reduced pressure. Crude ester was purified by silica gel column chromatography using CH_2Cl_2 as an eluent. Yield: 1.57 g (62%). Characterization data are the same as in ref. 15.

Synthesis of 2-cyano-6-pyrazol-1-yl-isonicotinic acid methyl ester (3) and 2-pyrazol-1-yl-6-(1*H*-tetrazol-5-yl)-isonicotinic acid methyl ester ($\mathbf{L^1H}$) was performed as detailed in ref. 15.

Synthesis of $[Fe(L^1)_2]$

Condition d. $\mathbf{L^1H}$ (0.0271 g, 0.1 mmol) was added to 21 ml of DCM and 9 ml of the MeOH mixture under Ar. To this 13.75 μl (0.1 mmol, slight excess) of Et_3N was added and stirred for 15 min. To this $Fe(BF_4)_2{\cdot}6H_2O$ (0.0168 g, 0.05 mmol) dissolved in 0.5 ml of MeOH was added and the mixture was stirred at room temperature for 2 h. A clear dark red solution was obtained which was filtered and kept for crystallization under ambient conditions. 22 mg (74%) of dark red crystals suitable for X-ray structural investigation were isolated after 2–3 weeks. Elemental analysis of the crystals: calc. for: $[\mathbf{Fe(L^1)_2}]{\cdot}0.4H_2O$ ($C_{22}H_{16.8}N_{14}O_{4.4}Fe$) C, 43.78; H, 2.81; N, 32.49; found: C, 43.78; H, 2.78; N, 32.33.

Condition e. $\mathbf{L^1H}$ (0.0542 g, 0.2 mmol) was added to 7 ml of DCM and 3 ml of the MeOH mixture under Ar. To this 27.5 μl (0.2 mmol) of Et_3N was added and stirred for 15 min. To this $Fe(BF_4)_2{\cdot}6H_2O$ (0.03375 g, 0.1 mmol) dissolved in 0.5 ml of MeOH was added and the mixture was stirred at room temperature for 2 h. A red precipitate was obtained which was filtered and washed with 2 × 5 ml of MeOH and dried under vacuum to yield 38 mg (64%) of dark red powder. Elemental analysis of the red powder: calc. for: $[\mathbf{Fe(L^1)_2}]{\cdot}1.3H_2O$ ($C_{22}H_{18.6}N_{14}O_{5.3}Fe$) C, 42.64; H, 3.03; N, 31.64; found: C, 42.68; H, 2.90; N, 31.58.

Instrumentation

X-ray crystallography

Single crystal X-ray diffraction data were collected on a STOE IPDS II diffractometer with graphite monochromated Mo-Kα radiation (0.71073 Å). The structures were solved by direct methods (SHELX-97). Refinement was performed with anisotropic temperature factors for all non-hydrogen atoms (disordered atoms were refined isotropically).

Photophysical measurements

UV-vis absorption spectral measurements were performed using a Varian Cary 5000 double-beam UV-vis-NIR spectrometer. The ligand and the complex were dissolved in the 7 : 3 dichloromethane (DCM)/methanol (MeOH) solvent mixture. Solution and solid phase PL measurements were performed on a Photon Technology International (PTI) spectrometer at ambient temperature. Relative quantum yields were measured using pyrene in ethanol (EtOH) as a reference (Q_F = 0.61). For solid state photo physical measurements the ligand and the complex were spin coated on Quartz substrates to obtain thin films and the coated substrates were dried under vacuum overnight to remove trapped solvents.

Magnetic measurements

All herein reported magnetic measurements were performed on an MPMS-XL7 SQUID magnetometer (Quantum Design). For standard magnetic measurements in the dark, the temperature dependent magnetization was recorded at B_{DC} = 1 T (crystalline sample) or 0.1 T (powder sample and all herein reported photomagnetic experiments) as an external magnetic field. The temperature sweeping rate was 0.3 K min^{-1} and it was the same for cooling and for heating modes. Every temperature data point was stabilised at a given temperature for 120 minutes before the own measurement. A gelatine capsule (standard measurements in the dark) was used as a sample holder in the temperature range of 5 ↔ 400 K. The very small diamagnetic contribution of the gelatine capsule had a negligible contribution to the overall magnetization which was dominated by the sample. The diamagnetic corrections of the molar magnetic susceptibilities were applied using Pascal's constants. The photomagnetic measurements were performed by using a diode-pumped solid-state laser (DPSS) Kvant (λ = 637 nm or 532 nm, 300 mW) coupled through an optical fibre to the cavity of an MPMS SQUID and the power on the sample surface was adjusted to 10 mW cm^{-2}. For the photomagnetic experiments, a small amount of sample was introduced onto transparent tape and mounted into the sample holder. The exact weight of samples (*ca.* 0.1 mg) was obtained by weighting and also verified by the comparison of the thermal χT *vs.* T curve with that of a more accurately weighed sample of the same compound. After cooling to 10 K, the sample, now in the low spin state, was irradiated and the change in magnetisation was followed. When the saturation point had been reached (after *ca.* 300 min for crystalline and 120 min for powder polymorph), the light was switched off, the temperature was increased at a rate of 0.3 K min^{-1}, and the magnetisation was measured at 1 K intervals. The T(LIESST) value was determined from the minimum of the $\partial(\chi T)/\partial T$ *vs.* T curve for the relaxation process. For the detection of light induced thermal hysteresis (LITH), the sample was slowly cooled down to 10 K again, and then the magnetic field (0.1 T) and the light were switched on. Next, the temperature dependence of magnetisation was monitored during thermal cycling up to 100 K and back down to 10 K, at a rate of 0.3 K min^{-1}.

DSC and SAXS measurements

DSC measurements were performed using a TA Instruments DSCQ1000 instrument operating at a scanning rate of 0.5 °C min^{-1} on heating and on cooling. SAXS patterns were obtained with a linear monochromatic Cu $K_{\alpha 1}$ beam (λ = 1.5405 Å) obtained using a sealed-tube generator equipped with a bent quartz monochromator and a curved Inel CPS 120 counter gas-filled detector; periodicities up to 70 Å can be measured, and the sample temperature is controlled to within ±0.01 °C from 20 to 200 °C. The sample was filled in Lindemann capillaries and exposure times were varied between 1 and 24 hours.

Acknowledgements

Grant Agencies (France: Agence Nationale de la Recherche-Labex NIE 11-LABX-0058_NIE within the investissement d'Avenir program ANR-10-IDEX-0002-02; Slovakia: APVV-14-0078, APVV-14-0073 and VEGA 1/0522/14; and Germany: DFG Transregio TR88 "3Met") are acknowledged for the financial support.

References

1 (*a*) *Spin-Crossover Materials: Properties and Applications*, ed. M. A. Halcrow, Wiley, Chichester, 2013; (*b*) O. Kahn and C. J. Martinez, *Science*, 1998, **279**, 44–48; (*c*) J. Real, A. B. Gasper and M. C. Muñoz, *Dalton Trans.*, 2005, 2062–2079; (*d*) V. Ksenofontov, A. B. Gaspar and P. Gütlich, in *Spin Crossover in Transition Metal Compounds*, ed. P. Gütlich and H. A. Goodwin, Topics in Current Chemistry, 2004, 235, pp. 39–66; (*e*) E. Breuning, M. Ruben, J.-M. Lehn, F. Renz, Y. Garcia, V. Ksenofontov, P. Gütlich and E. Wegelius. K. Rissanen, *Angew. Chem., Int. Ed.*, 2000, 2504–2507; (*f*) S. Decurtins, P. Gütlich, C. P. Kohler, H. Spiering and A. Hauser, *Chem. Phys. Lett.*, 1984, **105**, 1–4; (*g*) A. Hauser, *Chem. Phys. Lett.*, 1986, **124**, 543; (*h*) T. G. Gopakumar, F. Matino, H. Naggert, A. Bannwarth, F. Tuczek and R. Bernd, *Angew. Chem., Int. Ed.*, 2012, **51**, 6262; (*i*) V. Meded, A. Bagrets, K. Fink, R. Chandrasekar, M. Ruben, F. Evers, A. Bernand-Mantel, J. S. Seldenthuis, A. Beukman and H. S. J. van der Zant, *Phys. Rev. B: Condens. Matter Mater. Phys.*, 2011, **83**, 245415.

2 (*a*) V. Niel, J. M. Martinez-Agudo, M. C. Muñoz, A. B. Gaspar and J. A. Real, *Inorg. Chem.*, 2001, **40**, 3838–3839; (*b*) K. S. Murray and C. J. Kepert, in *Spin Crossover in Transition Metal Compounds*, ed. P. Gütlich and H. A. Goodwin, Topics in Current Chemistry, 2004, **233**, pp. 195–228.

3 (*a*) O. Kahn, J. Krober and C. Jay, *Adv. Mater.*, 1992, **4**, 718; (*b*) L. G. Lavrenova, N. G. Yudina, V. N. Ikorskii, V. A. Varnek, I. M. Oglezneva and S. V. Larionov, *Polyhedron*, 1995, **14**(10), 1333–1337; (*c*) O. Sato, *Acc. Chem. Res.*, 2003, **36**, 692–700.

4 (*a*) B. Djukic and M. T. Lemaire, *Inorg. Chem.*, 2009, **48**, 10489–10491; (*b*) Y. Koo and J. R. Galán-Mascarós, *Adv. Mater.*, 2014, **26**(39), 6785–6789; (*c*) E. J. Devid, P. N. Martinho, M. V. Kamalakar, I. Šalitroš, Ú. Prendergast, J. F. Dayen, V. Meded, T. Lemma, R. González-Prieto, F. Evers, T. E. Keyes, M. Ruben, B. Doudin and S. J. van der Molen, *ACS Nano*, 2015, **9**, 4496–4507; (*d*) E. Ruiz, *Phys. Chem. Chem. Phys.*, 2014, **16**, 14–22; (*e*) A. Rotaru, I. A. Gural'skiy, G. Molnár, L. Salmon, P. Demont and A. Bousseksou, *Chem. Commun.*, 2012, **48**, 4163–4165.

5 (*a*) T. Miyamachi, M. Gruber, V. Davesne, M. Bowen, S. Boukari, L. Joly, F. Scheurer, G. Rogez, T. K. Yamada, P. Ohresser, P. Ohresser, E. Beaurepaire and W. Wulfhekel, *Nat. Commun.*, 2012, **3**, 1–6; (*b*) M. Cavallini, I. Bergenti, S. Milita, G. Ruani, I. Šalitroš, Z. R. Qu, R. Chandrasekar and M. Ruben, *Angew. Chem., Int. Ed.*, 2008, **47**, 8596–8600; (*c*) T. Matsumoto, G. N. Newton, T. Shiga, S. Hayami, Y. Matsui, H. Okamoto, R. Kumai, Y. Murakami and H. Oshio, *Nat. Commun.*, 2014, 3865; (*d*) G. Aromí, D. Aguilà, P. Gamez, F. Luisc and O. Roubeau, *Chem. Soc. Rev.*, 2012, **41**, 537–546; (*e*) F. Prins, M. Monrabal-Capilla, E. A. Osorio, E. Coronado and H. S. J. van der Zant, *Adv. Mater.*, 2011, **23**(13), 1545–1549.

6 L. Cambi and L. Szego, *Ber. Dtsch. Chem. Ges. B*, 1931, **64**, 2591.

7 (*a*) P. Gütlich and H. A. Goodwin, *Spin crossover in transition metal compounds I-III*, Top. Curr. Chem., 2004, vol. 233–235; (*b*) D. M. Halepto, *et al.*, *J. Chem. Soc., Chem. Commun.*, 1989, 1322–1323; (*c*) P. G. Sim and E. Sinn, *J. Am. Chem. Soc.*, 1981, **103**, 241–243; (*d*) S. Hayami, Y. Komatsu, T. Shimizu, H. Kamihata and Y. H. Lee, *Coord. Chem. Rev.*, 2011, **255**, 1981–1990; (*e*) M. Nihei, T. Shiga, Y. Maeda and H. Oshio, *Coord. Chem. Rev.*, 2007, **251**, 2606–2621; (*f*) M. A. Halcrow, *Chem. Soc. Rev.*, 2008, **37**, 278–289; (*g*) A. Bousseksou, G. Molnár, L. Salmon and W. Nicolazzi, *Chem. Soc. Rev.*, 2011, **40**, 3313–3335.

8 (*a*) P. Gütlich, A. B. Gaspar and Y. Garcia, *Beilstein J. Org. Chem.*, 2013, **9**, 342–391; (*b*) P. Gütlich and H. A. Goodwin, in *Spin Crossover in Transition Metal Compounds*, ed. P. Gütlich and H. A. Goodwin, Topics in Current Chemistry, 2004, **233**, pp. 1–47; (*c*) M. A. Halcrow, *Chem. Lett.*, 2014, **43**, 1178–1188.

9 (*a*) F. Grandjean, G. J. Long, B. B. Hutchinson, L. N. Ohlhausen, P. Neill and J. D. Holcomb, *Inorg. Chem.*, 1989, **28**, 4406–4414; (*b*) J. A. Real, M. C. Muñoz, J. Faus and X. Solans, *Inorg. Chem.*, 1997, **36**, 3008–3013; (*c*) N. Moliner, L. Salmon, L. Capes and M. C. Muñoz, *J. Phys. Chem. B*, 2002, **106**, 4276; (*d*) A. L. Thompson, A. E. Goeta, J. A. Real and M. C. Muñoz, *Chem. Commun.*, 2004, 1390–1391.

10 (*a*) H. Naggert, A. Bannwarth, S. Chemnitz, T. von Hofe, E. Quandt and F. Tuczek, *Dalton Trans.*, 2011, **40**, 6364; (*b*) T. G. Gopakumar, M. Bernien, H. Naggert, F. Matino, C. F. Hermanns, A. Bannwarth, S. Muhlenberend, A. Kruger, D. Kruger, F. Nickel, W. Walter, R. Berndt, W. Kuch and F. Tuczek, *Chem. – Eur. J.*, 2013, **19**, 15702; (*c*) T. Palamarciuc, J. C. Oberg, F. E. Hallak, C. F. Hirjibehedin, M. Serri, S. Heutz, J.-F. Letarda and P. Rosa, *J. Mater. Chem.*, 2012, **22**, 9690; (*d*) A. Pronschinske, R. C. Bruce, G. Lewis, Y. Chen, A. Calzolari, M. Buongiorno-Nardelli, D. A. Shultz, W. You and D. B. Dougherty, *Chem. Commun.*, 2013, **49**, 10446.

11 B. Schäfer, C. Rajnák, I. Šalitroš, O. Fuhr, D. Klar, C. Schmitz-Antoniak, E. Weschke, H. Wende and M. Ruben, *Chem. Commun.*, 2013, **49**, 10986–10988.

12 D. Gentili, N. Demitri, B. Schäfer, F. Liscio, I. Bergenti, G. Ruani, M. Ruben and M. Cavallini, *J. Mater. Chem. C*, 2015, **3**, 7836–7844.

13 D. Ghosh, P. Parida and S. Pati, *Appl. Phys. Lett.*, 2015, **106**, 193105.

14 F. Zeng and Z. Yu, *Organometallics*, 2009, **28**, 1855–1862.

15 K. S. Kumar, B. Schäfer, S. Lebedkin, L. Karmazin, M. Kappes and M. Ruben, 2015, *Dalton Trans.*, 2015, **44**, 15611–15619.

16 (*a*) W. E. Ford and M. A. J. Rodgers, *J. Phys. Chem.*, 1992, **96**, 2917–2920; (*b*) D. S. Tyson and F. N. Castellano, *J. Phys. Chem. A*, 1999, **103**, 10955–10960.

17 (*a*) Y. Chi and P.-T. Chou, *Chem. Soc. Rev.*, 2007, **36**, 1421–1431; (*b*) L. S. Forster, *Coord. Chem. Rev.*, 2006, **250**, 2023–2033.

18 A. K. Pal and G. S. Hanan, *Chem. Soc. Rev.*, 2014, **43**, 6184–6197.
19 A. Santoro, L. J. K. Cook, R. Kulmaczewski, S. A. Barrett, O. Cespedes and M. A. Halcrow, *Inorg. Chem.*, 2015, **54**, 682–693.
20 D. F. Zigler, M. C. Elvington, J. Heinecke and K. J. Brewer, *Inorg. Chem.*, 2006, **45**, 6565–6567.
21 (*a*) Y. Garcia, F. Robert, A. D. Naik, G. Zhou, B. Tinant, K. Robeyns, S. Michotte and L. Piraux, *J. Am. Chem. Soc.*, 2011, **133**, 15850–15853; (*b*) C. Piguet, E. Rivara-Minten, G. Bernardinelli, J.-C. G. Bünzli and G. Hopfgartner, *J. Chem. Soc., Dalton Trans.*, 1997, 421–433; (*c*) C. Edder, C. Piguet, J.-C. G. Bünzli and G. Hopfgartner, *Chem. – Eur. J.*, 2001, **7**, 3014–3024; (*d*) M. Matsuda, H. Isozaki and H. Tajima, *Chem. Lett.*, 2008, **37**, 374–375; (*e*) L. Salmon, G. Molnar, D. Zitouni, C. Quintero, C. Bergaud, J.-C. Micheau and A. Bousseksou, *J. Mater. Chem.*, 2010, **20**, 5499–5503; (*f*) S. Titos-Padilla, J. M. Herrera, X.-W. Chen, J. J. Delgado and E. Colacio, *Angew. Chem., Int. Ed.*, 2011, **50**, 3290–3293; (*g*) M. Hasegawa, F. Renz, T. Hara, Y. Kikuchi, Y. Fukuda, J. Okubo, T. Hoshi and W. Linert, *Chem. Phys.*, 2002, **277**, 21–30; (*h*) C. A. Tovee, C. A. Kilner, J. A Thomas and M. A. Halcrow, *CrystEngComm*, 2009, **11**, 2069–2077; (*i*) L. J. K. Cook and M. A. Halcrow, *Polyhedron*, 2015, **87**, 91–97; (*j*) R. Gonzalez-Prieto, B. Fleury, F. Schramm, G. Zoppellaro, R. Chandrasekar, O. Fuhr, S. Lebedkin, M. Kappes and M. Ruben, *Dalton Trans.*, 2011, **40**, 7564–7570.
22 C. Lochenie, K. G. Wagner, M. Karg and B. Weber, *J. Mater. Chem. C*, 2015, **3**, 7925–7935.
23 I. Suleimanov, O. Kraieva, J. Sánchez Costa, I. O. Fritsky, G. Molnár, L. Salmon and A. Bousseksou, *J. Mater. Chem. C*, 2015, **3**, 5026–5032.
24 C.- F. Wang, R.-F. Li, X.-Y. Chen, R.-J. Wei, L.-S. Zheng and J. Tao, *Angew. Chem., Int. Ed.*, 2015, **54**, 1574–1577.
25 J.-F. Létard, P. Guionneau, L. Rabardel, J. A. K. Howard, A. E. Goeta, D. Chasseau and O. Kahn, *Inorg. Chem.*, 1998, **37**, 4432–4441.
26 H. Naggert, J. Rudnik, L. Kipgen, M. Bernien, F. Nickel, L. M. Arruda, W. Kuch, C. Nather and F. Tuczek, *J. Mater. Chem. C*, 2015, **3**, 7870–7877.
27 (*a*) A. Hauser, *J. Chem. Phys.*, 1991, **94**(4), 2741–2748; (*b*) P. Gütlich, A. Hauser and H. Spiering, *Angew. Chem., Int. Ed.*, 1994, **33**, 2024–2054.
28 M. Cavallini, I. Bergenti, S. Milita, J. C. Kengne, D. Gentili, G. Ruani, I. Salitros, V. Meded and M. Ruben, *Langmuir*, 2011, **27**, 4076–4081.
29 (*a*) R. Vincent, S. Klyatskaya, M. Ruben, W. Wernsdorfer and F. Balestro, *Nature*, 2012, **488**, 357–360; (*b*) S. Thiele, F. Balestro, R. Ballou, S. Klyatskaya, M. Ruben and W. Wernsdorfer, *Science*, 2014, **344**, 1135–1138.

